Supporting Information

Pérez Navarro et al. 10.1073/pnas.1304334110

SI Materials and Methods

Photsystem II (PSII) core complex preparations from wild-type *Thermosynechococcus elongatus* (1) were isolated as described earlier (2–4). X-band samples were prepared with the following modifications. After the loading of the Ni column with the solubilized membranes, the resin was washed with buffer 2 [1 M betaine, 10% (wt/vol) glycerol, 40 mM Mes, 15 mM $MgCl_2$, 15 mM $CaCl_2$, 100 mM NaCl, 1 mM L-histidine, 0.03% (wt/vol) β-DM, pH 6.5] until the optical density of the eluate at 665 nm decreased below 0.05 (~15 h). Then, PSII core complexes were eluted with buffer 3 [1 M betaine, 40 mM Mes, 15 mM $MgCl_2$, 15 mM $CaCl_2$, 200 mM NaCl, 180 mM L-histidine, 0.06% (wt/vol) β-DM, pH 6.5]. The eluate was then concentrated and washed in buffer 4 (1 M betaine, 15 mM $MgCl_2$, and 15 mM $CaCl_2$) by using centrifugal filter devices (Ultrafree-15; Millipore) until the Mes concentration was estimated to be lower than 0.5 mM. ^{15}N–labeled PSII samples were prepared from cells grown in a medium with $^{15}NH_4Cl$ and $^{15}NO_3$- salts. PSII core complexes were finally resuspended in buffer 4 (+ 40 mM Mes) at a Chl concentration of ~2–3 mg Chl·ml^{-1} and stored in liquid N_2 until use. PSII material for Q/W-band measurements was instead stored at −80 °C until use. The S_2 state was generated by short (5 s) white-light illumination with a tungsten lamp at 200 K, using an ethanol bath cooled down with dry ice. Resuspension of the PSII samples in labeled $H_2{}^{17}O$ (90%) buffer was achieved as reported in ref. 5. Ammonia was added at a ratio of 1:10 vol/vol to the samples from a stock solution of 1 M ammonium chloride ($^{14}NH_4Cl$) in 1 M Hepes (pH 7.6) buffer, yielding a free-base NH_3 concentration of 2 mM. PSII samples were reconcentrated using Millipore microcentrifuge filters to the desired concentration. Samples were then placed in Q/W-band tubes and left in complete darkness for ~10 min. To observe a minimally perturbed S_2 multiline signal, the sample was illuminated at 185 K (ethanol/liquid N2 bath). To observe the ammonia-modified multiline, the sample was first illuminated at 200 K and then subsequently annealed at ~260 K (ethanol + CO2/dry ice bath) for 30 s before freezing to 80 K. X-band samples were given two saturating YAG (532 nm) light flashes and 1 h dark adaptation before the addition of $^{14}NH_4Cl$ solution to maximize S_2 state yields.

Time-resolved membrane inlet mass spectrometry (TR-MIMS) experiments were performed in a stirred, temperature-controlled (20 °C) membrane-inlet cell (165 μL volume) connected to a magnetic sector field isotope ratio mass spectrometer (ThermoFinnigan Delta^{Plus} XP) via a cooling trap (liquid N_2). Samples were loaded in darkness. After 20 min of degassing, the sample was advanced to the S_2 state with one saturating Xe-lamp flash. Subsequently the sample was rapidly diluted with $H_2{}^{18}O$ (97%, 8 ms mixing time) and two further flashes were applied (interflash separation 10 ms), generating O_2. The delay between the dilution and the double flash was incremented between 8 ms and 10 s. The final ^{18}O sample enrichment was 22%. Molecular oxygen dissolved in the $H_2{}^{18}O$ was removed from the delivery syringe (modified Hamilton CR-700-50) by glucose/glucose oxidase and catalase (6). After 5 min, four additional flashes were given at 2 Hz and used for normalization. Data analysis was performed as described earlier (6–8).

Density functional theory calculations used an initial model geometry taken from Ames et al. (9) (model 1d2′ of that study), and were performed with the quantum chemical program system "ORCA" (28). This structure was reoptimized for the ammonia-modified S_2 state, after replacement of W1 with NH_3 (1d2′-NH_3) (Table S5). Geometry optimizations used the BP86 functional (10, 11) along with the 2010 dispersion corrections of Grimme (12) and the zero-order regular approximation (ZORA) to account for scalar relativistic effects (13–15). All atoms except carbon and hydrogen, for which the split-valence polarized SVP basis set was used, were described with the relativistically recontracted def2-TZVP(-f) basis sets (16). Decontracted def2-TZVP/J basis sets (17) were used for the resolution of the identity approximation to Coulomb exchange (RI-J). Tight self-consistent field (SCF) convergence and regular integration grids (Grid4 in ORCA convention) were applied. Optimizations were performed with the conductor-like screening model (COSMO) (18) with a dielectric constant of 8.0. Harmonic vibrational frequencies were computed for the optimized geometries, using numerical two-side differentiation with an increment of 0.01 Bohr. Both structures, with and without NH_3, were confirmed as genuine minima by the absence of imaginary frequencies (negative Hessian eigenvalues).

Exchange coupling constants were computed by the broken symmetry (BS)-DFT approach, using the TPSSh functional (19) with the RI-J approximation to the Coulomb exchange and the chain-of-spheres approximation to exact exchange (20). Scalar relativistic effects were included with ZORA paired with the segmented all-electron relativistically contracted (SARC) def2-TZVP(-f) basis sets and the decontracted def2-TZVP/J Coulomb fitting basis sets for all atoms. Increased integration grids (Grid5 and GridX5) were used in the calculation of all magnetic parameters. For the calculation of the hyperfine tensors, specially constructed basis sets based on SARC def2-TZVP but with added flexibility in the core region were used for the N and O atoms. These basis sets are described in ref. 21. The radial integration grids were increased to an integration accuracy of 9 (in ORCA convention) for ^{14}N and ^{17}O. Picture change effects were included in the calculation of EPR parameters. Details regarding the application of the BS-DFT approach for the calculation of EPR parameters in manganese systems can be found in recent work (9, 22–27).

SI EPR Theory/Simulations

EPR and ^{55}Mn-Electron Nuclear Double Resonance Data and Spin Hamiltonian Simulations. Spectra were simultaneously fitted assuming an effective spin $S = 1/2$ ground state (for details, see refs. 26, 29). The basis set that describes the Mn-tetramer spin manifold can be built from the product of the eigenstates of the interacting spins:

$$|\tfrac{1}{2} M I_1 I_2 I_3 I_4 m_1 m_2 m_3 m_4\rangle. \qquad \text{[S1]}$$

Here, M_i refers to the electronic magnetic sublevel, ±1/2; I_i takes the value 5/2 for each ^{55}Mn; and each m_i takes the values $-I_i$, $1 - I_i$, ... , $I_i - 1$, I_i.

The spin Hamiltonian that describes the spin manifold is

$$\hat{H} = \beta_e \vec{B}_0 \cdot \hat{G} \cdot \vec{S} + \sum_i \left(g_n \beta_n \vec{B}_0 \cdot \vec{I}_i + \vec{S} \cdot \hat{A}_i \cdot \vec{I}_i \right). \qquad \text{[S2]}$$

It contains (*i*) the electronic Zeeman term for the total electronic spin, (*ii*) nuclear Zeeman terms for the ^{55}Mn nuclei, and (*iii*) hyperfine terms for the ^{55}Mn nuclei. This Hamiltonian was used to simulate all spectra. The electron Zeeman term was treated exactly. The nuclear Zeeman and hyperfine terms were treated using second-order perturbation theory. The nuclear quadrupole coupling was not explicitly considered. Spectral simulations were performed numerically, using the EasySpin package (30) in MATLAB.

Historically, ammonia binding was thought to significantly alter the electronic structure of the oxygen-evolving complex (OEC), as proposed by Peloquin et al. (29). There, it was suggested that NH_3 binding led to an interchange of the valence states of the Mn cluster such that the only Mn in the +III oxidation state was located at a different Mn site (29). This proposal now seems unlikely. As shown in the main text, the Mn_{D1}-His332 signal, which can be considered a spin probe of the electronic structure of the OEC, does not significantly change upon NH_3 binding, requiring that the oxidation state of Mn_{D1}, the most likely candidate for the Mn^{III}, does not change (9, 26, 27, 31, 32). The effect of NH_3 binding is probably more similar to that seen upon the replacement of the Ca^{2+} ion with Sr^{2+}. Sr^{2+} has only a subtle effect on the electronic structure of the OEC, perturbing the $Mn_{D1}{}^{III}$ ion, which leads to changes in the hyperfine tensor anisotropy of all four Mn nuclei and thus a modified S_2 multiline EPR spectrum (26). Simulations of the EPR and ^{55}Mn-electron nuclear double resonance (ENDOR) data are shown in Fig. S1 and support this basic model. The fitted g and hyperfine tensors reported in Table S1 are approximately the same in terms of both magnitude and symmetry in both the control and the NH_3 sample, confirming that the oxidation state pattern for the OEC does not change upon ammonia binding, consistent with the ^{14}N-electron spin echo envelope modulation (ESEEM) Mn_{D1}-His332 data shown in Fig. 2 *C* and *D* in the main text.

^{14}N-ESEEM/^{17}O-Electron–Electron Double-Resonance–Detected NMR Data and Spin Hamiltonian Simulations. Spectra were simultaneously fitted assuming an effective spin $S = 1/2$ ground state (for details, see ref. 5). The basis set that describes the ligand-Mn-tetramer spin manifold (excluding ^{55}Mn nuclei) can be built from the product of the eigenstates of the interacting spins:

$$|\tfrac{1}{2} \quad M \quad I \quad m\rangle. \qquad \textbf{[S3]}$$

Here M refers to the electronic magnetic sublevels $\pm 1/2$; I takes the value 1 for ^{14}N and 5/2 for ^{17}O; and m_i takes the values $-I_i$, $1 - I_i$, ... , $I_i - 1$, I_i.

The spin Hamiltonian that describes the single nucleus–electron spin manifold is

$$\hat{H} = \beta_e \vec{B}_0 \cdot \hat{G} \cdot \vec{S} + g_o \beta_n \vec{B} \cdot \vec{I} + \vec{S} \cdot \hat{A} \cdot \vec{I}. \qquad \textbf{[S4]}$$

It contains (*i*) the electronic Zeeman term for the total electronic spin, (*ii*) the nuclear Zeeman term for the ^{14}N/^{17}O nucleus, and (*iii*) the hyperfine term for the ^{14}N/^{17}O nucleus. This Hamiltonian was used to simulate all ^{14}N-ESEEM spectra and ^{17}O-electron–electron double-resonance–detected NMR (EDNMR) data.

X-band three-pulse ESEEM measurements were performed on both ^{14}N-PSII and ^{15}N-PSII treated with ammonia ($^{14}NH_3$). As PSII contains additional cofactors such as cyt_{b559} and cyt_{c550}, which also exhibit nitrogen couplings, annealed-minus-dark difference spectra are reported. The annealed S_2 spectrum is generated by low-temperature illumination (185–200 K) and subsequent annealing to allow the ammonia to bind (260 K), whereas the dark S_1 spectrum represents the initial state. Nitrogen signals attributable to the OEC are seen only in the S_2 state whereas the cyt_{b559} and cyt_{c550} nitrogen signals should be unchanged in both S_1 and S_2. The annealed-minus-dark subtraction introduced no artifacts as evidenced by the comparison of the ^{14}N-PSII and universally labeled ^{15}N-PSII data, which are essentially identical. The annealed-minus-dark difference spectrum is assigned to a single ^{14}N of the Mn_4O_5Ca cluster-bound ammonia. This species displays three sharp nuclear-quadrupole lines at ∼0.5, 1.0, and 1.5 MHz in the Fourier-transformed spectra. Spin Hamiltonian simulations of the ESEEM spectra, measured at a series of τ-values, are shown in Fig. S2, *Left* and all fitted parameters are given in Table S2 along with DFT estimates for the hyperfine and quadrupole couplings. Our DFT calculations nominally reproduce the small experimental isotropic hyperfine coupling and the magnitude of the quadrupole coupling/electric field gradient. A multipole estimate was used to estimate the through-space interaction (A_{dip}), which suggests A_{dip} should be approximately axially symmetric, as observed experimentally. This simple calculation does, however, overestimate A_{dip} by a factor of 2.

The fitted spin Hamiltonian parameters of the $^{14}NH_3$ coupling reported in Table S2 are similar to those reported in the earlier higher-plant study (33). As seen in this earlier study, the quadrupole coupling shows significant asymmetry ($\eta \approx 0.5$). The recent crystal structure provides a rationale for this anomalous result, assuming NH_3 displaces the W1 ligand. W1 is in H-bonding distance to the D1-Asp61 and the Asp61/W1 couple has been proposed as important for proton movement from the OEC (34–36). Thus, an NH_3 ligand in the site of W1 is likely to have an electrostatic environment that is distorted away from axial symmetry. The role of such counter ions has recently been shown to be important for the calculation of quadrupole couplings of Mn complexes (21). As Asp61 is not included in our DFT models, this asymmetry is not reproduced in our calculations, although the magnitude of the quadrupole coupling is reproduced.

As a final proof that this signal represents a $^{14}NH_3$ ligand to the OEC, $^{15}NH_3$ instead of $^{14}NH_3$ was added to ^{14}N-PSII. In annealed-minus-dark difference spectra, the modulation described above was lost, replaced with transitions that now appear near 0 MHz in the Fourier-transformed spectra, consistent with a ^{15}N ligand interaction.

Spin Hamiltonian simulations were also performed for the ^{14}N-His332 signal seen using Q-band ESEEM, shown in Fig. S2, *Right*. A complete parameter list is given in Table S2 and compared with earlier literature data along with DFT estimates for the hyperfine and quadrupole couplings. As with the NH_3 ligand, our DFT calculations nominally reproduce the experimental isotropic hyperfine coupling and quadrupole coupling, and the DFT values are not significantly changed by the replacement of W1 with NH_3. It is noted that the fitted parameters are slightly different from those of our previous report using W-band EDNMR (5) but are similar to those of earlier ESEEM studies of Yeagle et al. (37) and Stich et al. (38), measured using PSII purified from spinach and *Synechocystis* (6803), respectively. This is currently under investigation and may reflect partial breakdown of the $S = 1/2$ ground-state approximation at W-band. In addition, current simulations do not very well reproduce ESEEM data traces collected using longer τ-values (>300 ns) compared to those with shorter τ-values (<300 ns). This is also being further investigated.

^{1}H-ENDOR. Protons in the vicinity of the OEC can be readily measured using Q-band ^{1}H-ENDOR (5). The magnitude of a proton coupling within a metallocofactor is usually derived from a simple dipolar (through-space) interaction between the electron spin and the nearby proton spin and thus allows the distance of the proton to the metal center(s) to be obtained. The width of the ^{1}H-ENDOR signal envelope (of ≈9 MHz) for the OEC in the S_2 state has previously been assigned to the terminal water/OH-ligands (W1/W2) of Mn_{A4}, i.e., ^{1}H protons ∼2.4–3 Å away from one of the Mn ions of the OEC that carries a spin projection of ∼1 (5, 39–41). In addition, the width of the envelope has been suggested to exclude a protonated oxygen bridge (μ-hydroxo).

The ^{1}H-ENDOR envelopes for ^{14}N-PSII with and without ammonia ($^{14}NH_3$) are shown in Fig. S3*A*. The two are very similar, suggesting that the nearest approach of a ^{1}H nucleus to the Mn ions is essentially the same for the OEC with and without an NH_3 ligand. In our DFT models, the protons of both the NH_3 and the W1/W2 ligands are between 2.4 and 2.7 Å away from Mn_{A4}. As such, the ^{1}H-ENDOR envelope is expected to not change considerably upon addition of ammonia, as observed

experimentally. Importantly, the absence of a large proton coupling suggests ammonia does not replace one of the oxygen bridges (μ-oxo) of the OEC, forming an amido (-NH_2-) bridge as previously suggested in ref. 33.

^{17}O-Mims ENDOR. Water molecules that are not directly coordinated to the Mn ions are not well visualized by using W-band EDNMR, and they provide only a small contribution to the signal envelope (5). These species, i.e., the waters bound to the Ca^{2+} ion, W3 and W4, can instead be measured using W-band Mims ENDOR (5). Fig. S3*B* shows the ^{17}O-Mims ENDOR spectra of W3/W4 in PSII samples with and without added ammonia. In both samples, a similar signal envelope is observed centered at the Lamor frequency of ^{17}O [$\nu_N(^{17}O) \approx 19.6$ MHz], suggesting ammonia does not displace W3 or W4. The signal has a width of <1 MHz (FWHM) and a near-Lorentzian lineshape, with a resolved splitting of 0.5 MHz.

^{17}O-EDNMR Simulations/Power Dependence. Spin Hamiltonian simulations of the EDNMR signals in Fig. 3 (^{14}N-PSII) and Fig. S4 (^{15}N-PSII) were performed as described in ref. 5. All parameters are given in Table S3. The anisotropic (dipolar, A_{dip}) component for each of the three ^{17}O hyperfine tensors (large, intermediate, and matrix) was kept fixed to that reported in ref. 5 in both the native and the ammonia-treated samples along with all linewidths. It is noted that the fitted linewidths presumably represent the unresolved quadrupole splittings. In addition, the unresolved quadrupole is expected to lead to the nonequal peak intensities for the double-quantum peaks of each ^{17}O doublet. As such, the relative intensities of each doublet peak are allowed to vary by 50%.

As the ^{17}O double-quantum region for the ammonia-treated sample was symmetric about twice the ^{17}O Larmor frequency, only two hyperfine couplings (large and intermediate) needed to be included to reproduce the double-quantum spectral profile.

In the ^{17}O-EDNMR experiments described here, the line intensities of the three different ^{17}O species predominately depend on the magnitude of the anisotropic (dipolar) coupling A_{dip} (5, 42) and the amplitude of the pump pulse [high turning angle (HTA) pulse]. As such, the relative line intensity attributable to different ^{17}O species will change as the amplitude of the HTA pulse is varied. In Rapatskiy et al. (5), the amplitude of the HTA pulse was set such that the signal from the largest coupled species was maximal. Increasing the amplitude of the HTA pulse begins to suppress the largest coupled species relative to more weakly coupled species; it effectively enhances the contribution of the more weakly coupled components. Thus, by monitoring the power dependence (the magnitude of the EDNMR signal as a function of the HTA pulse amplitude) at different positions within the signal envelope, more information on the contribution of each species can be obtained. In a simple sense, the power dependence represents another way to discern the number of species that make up the signal envelope. Unfortunately, the power dependence cannot yet be simulated, and thus, the contribution of each ^{17}O component is simply fitted (5).

The power dependence of the ^{17}O-EDNMR envelope is shown in Fig. S4 *C* and *D*. In the control sample, the power dependence of the satellite lines (strongly coupled species) about the ^{17}O Larmor frequency was significantly different from that of the central line (weakly coupled, matrix species) at the ^{17}O Lamor frequency. This is in contrast to the ammonia-treated sample. Here the power dependences of the satellites and the central line are more similar, suggesting the range of couplings that make up the envelope has decreased. That is to say, the ^{17}O profile in the ammonia-treated sample contains a smaller contribution from a third matrix component, i.e., W1.

1. Sugiura M, Boussac A, Noguchi T, Rappaport F (2008) Influence of histidine-198 of the D1 subunit on the properties of the primary electron donor, P680, of photosystem II in *Thermosynechococcus elongatus*. *Biochim Biophys Acta* 1777(4):331–342.
2. Boussac A, et al. (2004) Biosynthetic Ca^{2+}/Sr^{2+} exchange in the photosystem II oxygen-evolving enzyme of *Thermosynechococcus elongatus*. *J Biol Chem* 279(22):22809–22819.
3. Sander J, et al. (2010) Functional characterization and quantification of the alternative PsbA copies in *Thermosynechococcus elongatus* and their role in photoprotection. *J Biol Chem* 285(39):29851–29856.
4. Nowaczyk MM, et al. (2012) Deletion of *psbJ* leads to accumulation of Psb27-Psb28 photosystem II complexes in *Thermosynechococcus elongatus*. *Biochim Biophys Acta* 1817(8):1339–1345.
5. Rapatskiy L, et al. (2012) Detection of the water binding sites of the oxygen-evolving complex of Photosystem II using W-band ^{17}O ELDOR-detected NMR spectroscopy. *J Am Chem Soc* 134(40):16619–16634.
6. Messinger J, Badger M, Wydrzynski T (1995) Detection of one slowly exchanging substrate water molecule in the S_3 state of photosystem II. *Proc Natl Acad Sci USA* 92(8):3209–3213.
7. Hillier W, Messinger J, Wydrzynski T (1998) Kinetic determination of the fast exchanging substrate water molecule in the S_3 state of photosystem II. *Biochemistry* 37(48):16908–16914.
8. Hillier W, Wydrzynski T (2004) Substrate water interactions within the Photosystem II oxygen evolving complex. *Phys Chem Chem Phys* 6(20):4882–4889.
9. Ames W, et al. (2011) Theoretical evaluation of structural models of the S_2 state in the oxygen evolving complex of Photosystem II: Protonation states and magnetic interactions. *J Am Chem Soc* 133(49):19743–19757.
10. Perdew JP (1986) Density-functional approximation for the correlation energy of the inhomogeneous electron gas. *Phys Rev B Condens Matter* 33(12):8822–8824.
11. Becke AD (1988) Density-functional exchange-energy approximation with correct asymptotic behavior. *Phys Rev A* 38(6):3098–3100.
12. Grimme S, Antony J, Ehrlich S, Krieg H (2010) A consistent and accurate ab initio parametrization of density functional dispersion correction (DFT-D) for the 94 elements H-Pu. *J Chem Phys* 132(15):154104–154119.
13. van Lenthe E, Baerends EJ, Snijders JG (1993) Relativistic regular two-component Hamiltonians. *J Chem Phys* 99(6):4597–4610.
14. Van Lenthe E, Baerends EJ, Snijders JG (1994) Relativistic total-energy using regular approximations. *J Chem Phys* 101(11):9783–9792.
15. Van Wüllen C (1998) Molecular density functional calculations in the regular relativistic approximation: Method, application to coinage metal diatomics, hydrides, fluorides and chlorides, and comparison with first-order relativistic calculations. *J Chem Phys* 109:392–399.
16. Pantazis DA, Chen XY, Landis CR, Neese F (2008) All-electron scalar relativistic basis sets for third-row transition metal atoms. *J Chem Theory Comput* 4(6):908–919.
17. Weigend F (2006) Accurate Coulomb-fitting basis sets for H to Rn. *Phys Chem Chem Phys* 8(9):1057–1065.
18. Klamt A, Schüürmann D (1993) COSMO: A new approach to dielectric screening in solvents with explicit expressions for the screening energy and its gradient. *J Chem Soc Perk T* 2:799–805.
19. Staroverov VN, Scuseria GE, Tao J, Perdew JP (2003) Comparative assessment of a new nonempirical density functional: Molecules and hydrogen-bonded complexes. *J Chem Phys* 119:12129–12137.
20. Neese F, Wennmohs F, Hansen A, Becker U (2009) Efficient, approximate and parallel Hartree–Fock and hybrid DFT calculations. A 'chain-of-spheres' algorithm for the Hartree–Fock exchange. *Chem Phys* 356(1–3):98–109.
21. Cox N, et al. (2011) Electronic structure of a weakly antiferromagnetically coupled $Mn^{II}Mn^{III}$ model relevant to manganese proteins: A combined EPR, ^{55}Mn-ENDOR, and DFT study. *Inorg Chem* 50(17):8238–8251.
22. Pantazis DA, et al. (2009) A new quantum chemical approach to the magnetic properties of oligonuclear transition-metal complexes: Application to a model for the tetranuclear manganese cluster of photosystem II. *Chemistry* 15(20):5108–5123.
23. Orio M, Pantazis DA, Petrenko T, Neese F (2009) Magnetic and spectroscopic properties of mixed valence manganese(III,IV) dimers: A systematic study using broken symmetry density functional theory. *Inorg Chem* 48(15):7251–7260.
24. Neese F, et al. (2010) Dealing with complexity in open-shell transition metal chemistry from a theoretical perspective: Reaction pathways, bonding, spectroscopy, and magnetic properties. *Adv Inorg Chem* 62:301–349.
25. Pantazis DA, Ames W, Cox N, Lubitz W, Neese F (2012) Two interconvertible structures that explain the spectroscopic properties of the oxygen-evolving complex of photosystem II in the S_2 state. *Angew Chem Int Ed Engl* 51(39):9935–9940.
26. Cox N, et al. (2011) Effect of Ca^{2+}/Sr^{2+} substitution on the electronic structure of the oxygen-evolving complex of photosystem II: A combined multifrequency EPR, ^{55}Mn-ENDOR, and DFT study of the S_2 state. *J Am Chem Soc* 133(10):3635–3648.
27. Pantazis DA, et al. (2009) Structure of the oxygen-evolving complex of photosystem II: Information on the S_2 state through quantum chemical calculation of its magnetic properties. *Phys Chem Chem Phys* 11(31):6788–6798.
28. Neese F (2012) The ORCA program system. *Comput Mol Sci* 2(1):73–78.
29. Peloquin JM, et al. (2000) ^{55}Mn ENDOR of the S_2-state multiline EPR signal of photosystem II: Implications on the structure of the tetranuclear Mn cluster. *J Am Chem Soc* 122(44):10926–10942.
30. Stoll S, Schweiger A (2006) EasySpin, a comprehensive software package for spectral simulation and analysis in EPR. *J Magn Reson* 178(1):42–55.

31. Teutloff C, et al. (2009) Electronic structure of the tyrosine D radical and the water-splitting complex from pulsed ENDOR spectroscopy on photosystem II single crystals. *Phys Chem Chem Phys* 11(31):6715–6726.
32. Schinzel S, Schraut J, Arbuznikov AV, Siegbahn PE, Kaupp M (2010) Density functional calculations of ^{55}Mn, ^{14}N and ^{13}C electron paramagnetic resonance parameters support an energetically feasible model system for the S_2 state of the oxygen-evolving complex of photosystem II. *Chemistry* 16(34):10424–10438.
33. Britt RD, Zimmermann JL, Sauer K, Klein MP (1989) Ammonia binds to the catalytic manganese of the oxygen-evolving complex of photosystem II. Evidence by electron spin-echo envelope modulation spectroscopy. *J Am Chem Soc* 111(10):3522–3532.
34. Dilbeck PL, et al. (2012) The D1-D61N mutation in *Synechocystis* sp. PCC 6803 allows the observation of pH-sensitive intermediates in the formation and release of O_2 from photosystem II. *Biochemistry* 51(6):1079–1091.
35. Rivalta I, et al. (2011) Structural-functional role of chloride in photosystem II. *Biochemistry* 50(29):6312–6315.
36. Pokhrel R, McConnell IL, Brudvig GW (2011) Chloride regulation of enzyme turnover: Application to the role of chloride in photosystem II. *Biochemistry* 50(14):2725–2734.
37. Yeagle GJ, Gilchrist ML, Jr., Walker LM, Debus RJ, Britt RD (2008) Multifrequency electron spin-echo envelope modulation studies of nitrogen ligation to the manganese cluster of photosystem II. *Philos Trans R Soc Lond B Biol Sci* 363 (1494):1157–1166, discussion 1166.
38. Stich TA, Yeagle GJ, Service RJ, Debus RJ, Britt RD (2011) Ligation of D1-His332 and D1-Asp170 to the manganese cluster of photosystem II from *Synechocystis* assessed by multifrequency pulse EPR spectroscopy. *Biochemistry* 50(34):7390–7404.
39. Kawamori A, Inui T, Ono T, Inoue Y (1989) ENDOR study on the position of hydrogens close to the manganese cluster in S_2 state of photosystem II. *FEBS Lett* 254(1–2):219–224.
40. Aznar CP, Britt RD (2002) Simulations of the ^{1}H electron spin echo-electron nuclear double resonance and ^{2}H electron spin echo envelope modulation spectra of exchangeable hydrogen nuclei coupled to the S_2-state photosystem II manganese cluster. *Philos Trans R Soc Lond B Biol Sci* 357(1426):1359–1365, discussion 1365–1367.
41. Britt RD, et al. (2004) Recent pulsed EPR studies of the photosystem II oxygen-evolving complex: Implications as to water oxidation mechanisms. *Biochim Biophys Acta* 1655(1–3):158–171.
42. Schosseler P, Wacker T, Schweiger A (1994) Pulsed ELDOR detected NMR. *Chem Phys Lett* 224(3–4):319–324.

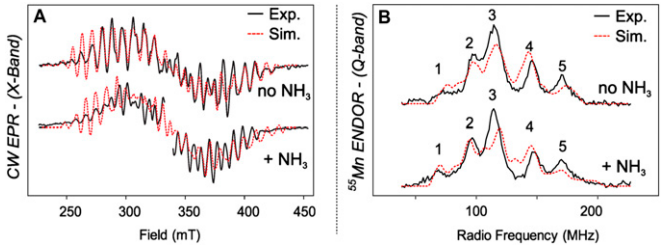

Fig. S1. X-band CW-EPR and Q-band pulse-EPR ^{55}Mn-ENDOR spectra of the control and NH_3-containing OEC of PSII derived from *Thermosynechococcus elongatus* poised in the S_2 state (1, 2). (*A*) X-band CW EPR. The S_1-state background of cyt b559 and cyt c550 was subtracted from the data after illumination. In native samples, a point mutation was made to replace the tyrosine Y_D (D2-Tyr160) with a phenylalanine, removing from the spectrum the $Y_D^\bullet$ signal. In samples, treated with ammonia, the $Y_D^\bullet$ signal, centered at about $g \approx 2$, was removed for clarity of presentation Experimental parameters: microwave frequencies, 9.4097 GHz (control) and 9.4075 GHz (NH_3); microwave power, 20 mW; modulation amplitude, 25 G; time constant, 80 ms; temperature, 8.6 K. (*B*) Q-band pulse ^{55}Mn-Davies ENDOR. The S_1-state spectrum was subtracted from the S_2-state data to remove a small Mn^{2+} contamination. Experimental parameters: microwave frequencies, 34.0368 GHz (native) and 34.0159 GHz (NH_3); magnetic field, 1,220 mT; shot repetition time, 1 ms; microwave pulse length (π), 24 ns; τ, 268 ns; radio frequency pulse (π_{RF}), 3.5 μs; temperature, 5.2 K. The red dotted lines represent a least-squares fitting to the whole dataset, using a model based on the spin Hamiltonian formalism. The optimized parameter sets are given in Table S2.

1. Boussac A, Sugiura M, Inoue Y, Rutherford AW (2000) EPR study of the oxygen evolving complex in His-tagged photosystem II from the cyanobacterium *Synechococcuselongatus*. *Biochemistry* 39(45):13788–13799.
2. Boussac A, Rutherford AW, Styring S (1990) Interaction of ammonia with the water splitting enzyme of photosystem II. *Biochemistry* 29(1):24–32.

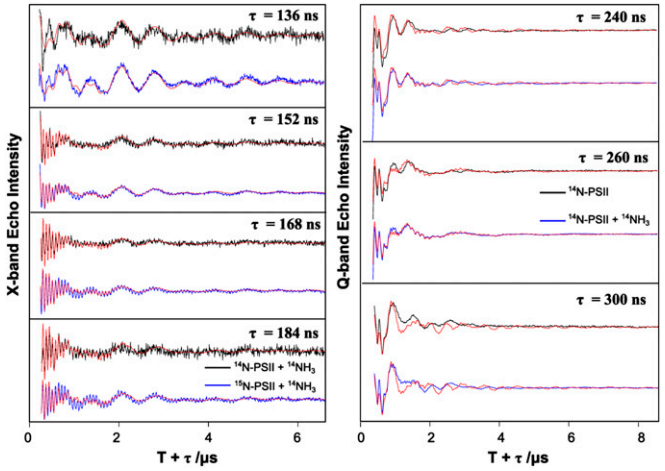

Fig. S2. (*Left*) X-band three-pulse ESEEM annealed-minus-dark difference spectra of ammonia ($^{14}NH_3$)-treated ^{14}N-PSII and ^{15}N-PSII (*SI Materials and Methods*). (*Right*) Q-band three-pulse ESEEM light-minus-dark and annealed-minus-dark difference spectra of control and ammonia ($^{14}NH_3$)-treated ^{14}N-PSII, respectively. Spectra were collected using the sequence t_p–τ–t_p–T–t_p–τ–echo, where the length of the $\pi/2$ microwave pulse was set to $t_p = 8$ ns (X-band) and $t_p = 12$ ns (Q-band); the interpulse distance (τ) was set to the values $\tau = 136$, 152, 168, and 184 ns (X-band) and $\tau = 240$, 260, and 300 ns (Q-band); and the interpulse distance (T) was swept over the range from 64 to 6,464 ns in steps of $\Delta T = 8$ ns (X-band) and from 100 to 8,176 ns in steps of $\Delta T = 16$ ns (Q-band). Experimental parameters: $B_0 =$ 333 mT (X-band), 1.22 T (Q-band); temperature, 4.2 K (X-band), 5.2 K (Q-band); shot repetition time of 5 ms (X-band), 1 ms (Q-band). The red dashed lines superimposing the data represent simulations using the spin Hamiltonian formalism (Table S4). The modulation due to protons in the X-band data was simulated using a single, isolated ^{1}H species. The decay of the ESEEM traces (data and simulations) was fitted to a third-order polynomial (X-band) and a biexponential decay (Q-band) function. A low-pass filter (3 dB, 10 MHz) was applied to the Q-band ESEEM simulations in an attempt to model the resonator bandwidth.

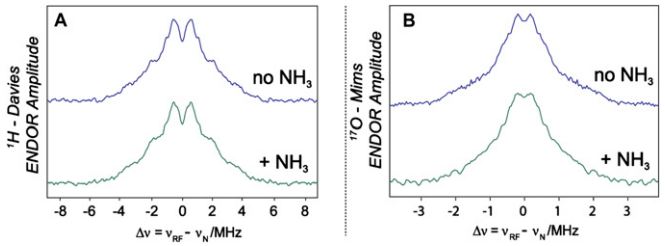

Fig. S3. Q-band ^{1}H- and W-band ^{17}O- ENDOR spectra of control and NH_3-treated ^{14}N-PSII of *Thermosynechococcus elongatus* poised in the S_2 state (200 K white light), exchanged in $H_2{}^{17}O$-based buffer in the S_1 state, measured at the center of the multiline EPR spectrum. Spectra were symmetrized around the Larmor frequency of the ^{1}H and ^{17}O nuclei, respectively. (*A*) Q-Band ^{1}H-Davies ENDOR. Spectra were acquired using the pulse sequence t_{inv}–t_{RF}–T–t_p–τ–2t_p–τ–echo, with an inversion microwave pulse of length t_{inv} = 128 ns and a radio frequency π pulse of length t_{RF}= 20 μs. The length of the $\pi/2$ microwave pulse in the detection sequence was set to t_p = 64 ns and the interpulse delays to T = 1.5 μs, τ = 468 ns, and temperature 5.2 K. The RF frequency was swept 20 MHz around the ^{1}H-Larmor frequency of about 53 MHz in 50-kHz steps. The magnetic field was B_0 = 1.22 T. (*B*) W-band ^{17}O-Mims ENDOR. Spectra were collected using the pulse sequence t_p–τ–t_p–t_{RF}–T–t_p–τ–echo, with t_p = 24 ns, t_{RF}= 14 μs, τ = 300 ns, T = 1 μs, and temperature 4.8 K. The RF frequency was swept 6.4 MHz around the ^{17}O-Larmor frequency of about 19.7 MHz in 43 kHz steps. The magnetic field was B_0 = 3.40 T.

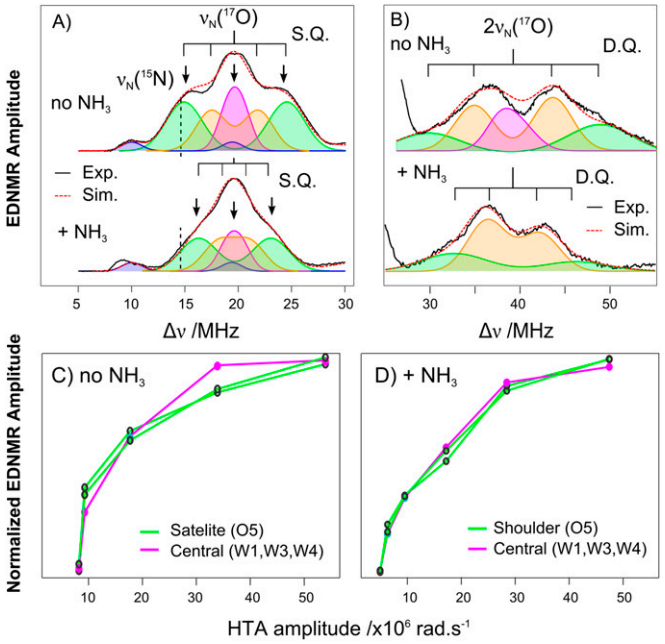

Fig. S4. (*A* and *B*) W-band EDNMR spectra and (*C* and *D*) HTA power dependence of the ^{17}O-EDNMR signal envelope of native ^{15}N-PSII (*A* and *B*, *Upper*, and *C*) and ^{15}N-PSII treated with NH_3 (*A* and *B*, *Lower*, and *D*). The black lines represent the data; the red dashed lines represent the summed simulations. Measurements were performed using the pulse sequence t_{HTA}–T–t_p–τ–2t_p–τ–echo. The high turning angle (HTA) microwave pulse was applied at microwave frequency ν_{mw}. The detection Hahn echo pulse sequence t_p–τ–2t_p–τ–echo at the microwave frequency $\nu_{mw}^{(0)}$, matched to the cavity resonance, was set 6 μs after the HTA pulse to ensure near-complete decay of the electron spin coherencies. The $\pi/2$ pulse length used for detection was t_p = 100 ns with an interpulse separation of τ = 500 ns. The echo was integrated 600 ns around its maximum. The spectra were acquired via continuously sweeping the HTA frequency ν_{mw} at fixed B_0 in steps of 68.4 kHz. The amplitude of the HTA microwave pulse was varied: $\omega_1 = 5–50 \times 10^6$ rad·s^{-1}. In Fig. 3 of the main text, a longer $\pi/2$ pulse (200 ns) and integration window (800 ns) and a shorter T of 1.5 μs were used. The amplitude of the HTA pulse was $\omega_1 \approx 10 \times 10^6$ rad·s^{-1}.

Table S1. Principal values of the effective *G* and hyperfine tensors (A_i) for the EPR and 55Mn-ENDOR simulations (Fig. S1)

			A_i, MHz		
Sample	*G*	A_1	A_2	A_3	A_4
Control					
x	1.988	321	259	191	161
y	1.978	345	244	219	179
z	1.974	273	272	249	230
iso	1.980	313	258	220	190
aniso	0.009	60	−20	−44	−60
$+NH_3$					
x	1.993	314	230	185	167
y	1.974	379	264	215	153
z	1.964	248	279	244	218
iso	1.981	321	246	209	170
aniso	0.019	98	−31	−44	−58

The isotropic $\boldsymbol{G}$ and $\boldsymbol{A}_i$ (i = 1–4) values are the average of the individual values: $\boldsymbol{G}_{iso} = (\boldsymbol{G}_x + \boldsymbol{G}_y + \boldsymbol{G}_z)/3$ and $\boldsymbol{A}_{i,iso} = (\boldsymbol{A}_{i,x} + \boldsymbol{A}_{i,y} + \boldsymbol{A}_{i,z})/3$. The anisotropy in the $\boldsymbol{G}$ and $\boldsymbol{A}_i$ values is expressed as the difference between equatorial (average of *x* and *y*) and the axial (*z*) components of the tensor.

Table S2. Fitted and DFT-calculated spin Hamiltonian parameters for the $^{14}NH_3$ ligand and the ^{14}N-His332 ligand of the OEC: Comparison with literature values

	Spin Hamiltonian parameters/MHz			
OEC ligand	$\lvert A_{iso}\rvert$	A_{dip}*	$\lvert e^2Qq/h\rvert$	η
$^{14}NH_3$				
Experiment	2.36	0.41, 0.26, −0.67	1.52	0.47
DFT 1d2′-NH_3[†]	1.46	0.78, 0.73, −1.51	2.52	0.06
(1)	2.29	0.2, 0.2, −0.4	1.61	0.59
^{14}N-His332				
Experiment	7.17	0.11, 1.43, −1.54	2.00[‡]	0.81
DFT 1d2′[†]	4.83	1.17, 0.97, −2.14	2.13	0.78
DFT 1d2′-NH_3[†]	5.23	1.16, 0.97, −2.13	2.15	0.77
(2)	6.95	0.2,1.3, −1.5	1.98[‡]	0.82

*Theoretical A_{dip} values represent a multipole estimate as described in Force et al. (3).

[†]The 1d2′ model as reported in Ames et al. (4). 1d2′-NH_3 is an optimized DFT model with NH_3 bound instead of W1.

[‡]The quadrupole tensor was rotated relative to the hyperfine tensor around the Euler angles $[\alpha \quad \beta \quad \gamma] = [0 \quad -13 \quad 26]^\circ$, similar to ref. 2, where $[\alpha \quad \beta \quad \gamma] = [-30 \quad 0 \quad 40]^\circ$.

1. Britt RD, Zimmermann JL, Sauer K, Klein MP (1989) Ammonia binds to the catalytic manganese of the oxygen-evolving complex of photosystem II. Evidence by electron spin-echo envelope modulation spectroscopy. *J Am Chem Soc* 111(10):3522–3532.
2. Stich TA, Yeagle GJ, Service RJ, Debus RJ, Britt RD (2011) Ligation of D1-His332 and D1-Asp170 to the manganese cluster of photosystem II from *Synechocystis* assessed by multifrequency pulse EPR spectroscopy. *Biochemistry* 50(34):7390–7404.
3. Force DA, Randall DW, Lorigan GA, Clemens KL, Britt RD (1998) ESEEM studies of alcohol binding to the manganese cluster of the oxygen evolving complex of photosystem II. *J Am Chem Soc* 120(51):13321–13333.
4. Ames W, et al. (2011) Theoretical evaluation of structural models of the S_2 state in the oxygen evolving complex of Photosystem II: Protonation states and magnetic interactions. *J Am Chem Soc* 133(49):19743–19757.

Table S3. Fitted spin Hamiltonian parameters for the exchangeable ^{17}O ligands of the OEC in the presence and absence of ammonia

	Fitted spin Hamiltonian parameters/MHz			BS-DFT calculations/ MHz	
				1d2′/1d2′-NH_3	
^{17}O signal	$\|A_{iso}\|$	A_{dip}	$A(\eta)$	$\|A_{iso}\|$	Site
Strong	9.7	2.2	0.55	—	—
Intermediate	4.5	0.6	0.08	5.20	W2
Matrix	1.4	0.6	0.06	1.69	W1
NH_3					
Strong	7.0	2.2	0.55	—	—
Intermediate	3.1	0.6	0.08	4.32	W2
Matrix	—	—	—	—	—

EDNMR linewidth for ^{17}O signals: strong, 3.5 MHz [single quantum (SQ)], 7.4 MHz [double quantum (DQ)]; intermediate, 3.3 MHz (SQ), 5.0 MHz (DQ); and matrix, 2.2 MHz (SQ), 3.8 MHz (DQ).

Table S4. Calculated ^{17}O μ-oxo bridge hyperfine couplings: Comparison with experimental parameters

			^{17}O μ-oxo bridge hyperfine couplings $\|A_{iso}\|$/MHz*				
Method	S_T	ΔE/cm^{-1}	O1	O2	O3	O4	O5
DFT							
1d2′[†]	1/2	25.6	0.52	23.05	4.90	4.48	17.41
1d2′-NH_3[†]	1/2	27.6	1.07	23.19	4.81	5.34	12.21
Δ[‡]	—	2.0	0.55	0.14	−0.09	0.86	−5.20
Δ, %[‡]		7.8	106	1	−2	19	−30
Experiment							
Native	1/2	—			9.7		
+NH_3	1/2	—					7.0
Δ[‡]	—	—			2.7		
Δ, %[‡]					−28 ≥ O5[§]		

ΔE, energy-gap between the ground and first excited spin state.

*Calculated (raw) BS-DFT hyperfine values are not directly comparable to experiment; the percentage change (Δ) due to ammonia binding can, however, be compared.

[†]The 1d2′ model as reported in Ames et al. (9). 1d2′-NH_3 is an optimized DFT model with NH_3 bound instead of W1.

[‡]Δ = difference between control and +NH_3 samples.

[§]The experimental 28% decrease in the oxo bridge hyperfine best matches O5.

Table S5. Optimized model geometries used for EPR parameter and vibrational frequency calculations

DFT model	*x*/Å	*y*/Å	*z*/Å
1d2′			
Atom			
Mn	29.19414	36.61847	65.00569
Mn	28.9668	36.43165	67.6823
Mn	29.01561	38.18004	69.82962
Mn	26.62394	38.66455	68.47251
Ca	29.67399	39.73626	66.98265
O	28.45455	37.61803	66.31241
O	30.00886	35.70723	66.38433
O	30.065	37.71235	68.40141
O	28.18288	39.5523	68.91232
O	27.66949	37.12485	68.98152
H	33.26521	35.97244	63.9053
C	33.39239	36.9531	63.41026
H	34.41265	36.98277	62.98899
C	33.18412	38.1003	64.4023
C	31.81431	38.16099	65.07295
O	31.64374	38.90592	66.0647
O	30.89382	37.43168	64.51395
H	23.41284	44.20104	66.83036
C	23.14235	43.30812	66.23537
H	22.05665	43.14138	66.35523
C	23.94833	42.07976	66.67913
C	25.46034	42.28601	66.52075
C	26.33971	41.10987	66.91852
O	27.54446	41.08187	66.55113
O	25.76884	40.18857	67.63863
H	20.97205	34.9217	66.73777
C	21.79667	34.56477	66.09691
C	22.62626	33.58101	66.91447
C	22.67446	35.75242	65.61673
C	23.51361	36.39167	66.68698
N	23.0952	36.51948	68.00583
C	24.74607	37.02593	66.64159
C	24.0326	37.18614	68.71421
N	25.04427	37.51441	67.90507
N	23.39158	32.71597	66.19706
C	24.54488	32.0307	66.78717
H	24.22685	31.56093	67.73365
C	25.70247	33.00813	67.05431
C	26.16809	33.7335	65.79022
C	27.20746	34.80999	66.03121
O	27.51408	35.11177	67.22407
O	27.70084	35.35641	64.97236
H	26.17566	32.17784	73.8084
C	26.68915	33.03106	74.28791
H	26.75269	32.8301	75.37319
C	25.94358	34.34991	74.00002
C	25.82893	34.64465	72.53042
N	24.80965	34.12276	71.74217
C	26.694	35.38315	71.73127
C	25.05611	34.54574	70.49867
N	26.18938	35.30448	70.44992
H	26.4334	38.28926	75.03005
C	26.97487	38.34995	74.06977
H	27.68597	39.19239	74.12322
C	25.99156	38.52463	72.91222
C	26.61796	38.59626	71.52631
O	27.89489	38.44788	71.45365
O	25.83464	38.77529	70.53788
C	31.08901	40.1793	70.05314
O	30.97748	40.51983	68.85136

Table S5. Cont.

DFT model	*x*/Å	*y*/Å	*z*/Å
O	30.3749	39.25827	70.64874
H	29.99232	32.54574	73.42881
C	30.76375	33.3375	73.4744
H	30.91634	33.59586	74.53747
C	30.35041	34.56855	72.65713
C	30.09602	34.22427	71.1855
C	29.74158	35.39481	70.287
O	29.66549	36.55887	70.81184
O	29.52166	35.11434	69.05342
O	22.66383	33.63393	68.16136
H	32.67821	37.01437	62.57016
H	23.33155	32.75652	65.18353
H	26.61089	35.81249	69.6557
H	27.71807	33.07295	73.886
H	23.32986	43.54911	65.17177
H	31.70671	32.90224	73.09335
H	33.92927	38.0708	65.21875
H	33.32378	39.08152	63.90671
H	26.46861	35.188	74.49708
H	24.92771	34.30805	74.43769
H	27.5877	35.9661	71.95071
H	24.43541	34.32991	69.6241
H	23.98054	37.41129	69.77896
H	25.42938	37.17442	65.80366
H	22.29504	36.04055	68.41472
H	24.84834	31.22744	66.09367
C	32.13206	40.82337	70.94596
H	31.72942	40.99882	71.9571
H	32.98563	40.12715	71.04144
H	32.48973	41.76537	70.50259
H	31.13148	35.34893	72.72075
H	29.43555	35.01892	73.08723
H	30.97619	33.72666	70.73253
H	29.26257	33.50016	71.08804
H	23.6431	41.19161	66.0929
H	25.72451	42.54924	65.47866
H	23.72577	41.83528	67.7343
H	25.8007	43.14371	67.13756
H	22.00871	36.51395	65.16539
H	21.34015	34.08152	65.21456
H	23.34942	35.42295	64.80618
H	27.56668	37.42592	73.94979
H	25.37142	39.4331	73.03447
H	25.2811	37.6758	72.86661
H	25.37514	33.75377	67.79815
H	25.31963	34.23982	65.2903
H	26.58269	33.03359	65.03991
H	26.54528	32.46101	67.5142
O	29.15439	40.05838	64.54705
H	28.33034	40.56792	64.68734
O	29.97389	35.2413	63.56888
H	28.83906	39.18103	64.15145
O	28.38338	37.64617	63.62991
H	30.38308	42.52047	67.5307
O	30.06619	42.18126	66.67075
H	29.11539	42.42716	66.63169
H	29.9559	34.34343	63.95881
H	30.92241	35.49688	63.55008
H	28.88879	37.52055	62.80245
1d2′-NH_3/Å			
Atom			
Mn	29.29261	36.50957	64.9875

Table S5. Cont.

DFT model	*x*/Å	*y*/Å	*z*/Å
Mn	28.98648	36.40715	67.6681
Mn	29.00729	38.16493	69.81606
Mn	26.62227	38.63982	68.44718
Ca	29.67254	39.67307	66.95789
O	28.51688	37.56202	66.28165
O	30.06033	35.64238	66.41896
O	30.07367	37.69387	68.40509
O	28.17571	39.53302	68.88591
O	27.66903	37.10738	68.95866
H	33.31983	36.17044	63.58316
C	33.39829	37.20513	63.20367
H	34.39817	37.32556	62.75046
C	33.19111	38.22033	64.33007
C	31.84324	38.16011	65.04645
O	31.65396	38.87759	66.0565
O	30.97386	37.35932	64.51055
H	23.55609	44.31083	66.93375
C	23.19282	43.41108	66.40176
H	22.11547	43.30319	66.62229
C	23.97751	42.16133	66.82366
C	25.47684	42.28632	66.52638
C	26.33717	41.08812	66.90027
O	27.53526	41.04033	66.51023
O	25.76184	40.17008	67.61834
H	20.95154	34.91649	66.71795
C	21.77922	34.55297	66.08483
C	22.60572	33.57914	66.91729
C	22.66027	35.73531	65.59725
C	23.49903	36.37805	66.6654
N	23.06983	36.53282	67.97785
C	24.74313	36.98931	66.62372
C	24.01223	37.19322	68.68578
N	25.03746	37.49167	67.8825
N	23.38138	32.71259	66.21249
C	24.53263	32.03754	66.81802
H	24.20968	31.58311	67.7703
C	25.68825	33.01949	67.07494
C	26.16888	33.71755	65.80114
C	27.23011	34.77704	66.03017
O	27.5407	35.08189	67.22172
O	27.73779	35.29945	64.96851
H	26.14555	32.16961	73.78782
C	26.65957	33.0178	74.2757
H	26.71895	32.80819	75.35961
C	25.91859	34.34085	73.99523
C	25.81064	34.64751	72.5275
N	24.78807	34.14226	71.73278
C	26.6856	35.38261	71.73592
C	25.04274	34.57228	70.49308
N	26.18356	35.31971	70.45285
H	26.39706	38.29622	75.00646
C	26.94253	38.35107	74.04803
H	27.65591	39.19167	74.10052
C	25.96476	38.52306	72.88541
C	26.59762	38.58903	71.50167
O	27.87441	38.44196	71.43485
O	25.81786	38.76315	70.50947
C	31.06272	40.18269	70.03568
O	30.95599	40.50991	68.82962
O	30.35447	39.26126	70.63699
H	29.98017	32.57898	73.48591
C	30.75442	33.36867	73.51841

Table S5. Cont.

DFT model	*x*/Å	*y*/Å	*z*/Å
H	30.91212	33.63988	74.57757
C	30.34207	34.59037	72.68664
C	30.08174	34.22837	71.22035
C	29.73268	35.3885	70.30494
O	29.65	36.55815	70.82011
O	29.52379	35.0971	69.07459
O	22.63212	33.64156	68.16378
H	32.64395	37.33271	62.40745
H	23.33231	32.74842	65.1982
H	26.61563	35.82718	69.6621
H	27.68996	33.06006	73.87756
H	23.29614	43.60325	65.31689
H	31.69436	32.9252	73.13928
H	33.96276	38.11455	65.11608
H	33.29138	39.25805	63.9558
H	26.44387	35.17345	74.50128
H	24.90083	34.29822	74.42841
H	27.58398	35.95587	71.96173
H	24.42251	34.36841	69.61547
H	23.95416	37.43523	69.74653
H	25.43716	37.11327	65.79072
H	22.25621	36.07664	68.38556
H	24.83963	31.22306	66.13913
C	32.09504	40.84653	70.92733
H	31.69138	41.0155	71.93913
H	32.9616	40.16622	71.02109
H	32.43528	41.79442	70.48261
H	31.12589	35.36899	72.73767
H	29.43042	35.0494	73.11437
H	30.95714	33.71789	70.77268
H	29.24247	33.5093	71.13545
H	23.58046	41.26812	66.30434
H	25.65847	42.48922	65.45299
H	23.83853	41.96767	67.90357
H	25.91014	43.15412	67.06524
H	21.99747	36.49542	65.13914
H	21.32706	34.05997	65.20558
H	23.33661	35.39808	64.7911
H	27.53211	37.42481	73.93458
H	25.34557	39.43297	73.00199
H	25.25336	37.67509	72.83987
H	25.35394	33.78164	67.79864
H	25.33028	34.23023	65.29115
H	26.57369	32.9981	65.06393
H	26.52601	32.48263	67.55564
O	29.1129	39.96224	64.51792
H	28.27681	40.44473	64.68325
H	28.81983	39.06806	64.14843
O	28.51217	37.49962	63.55323
H	30.34963	42.45934	67.47842
O	30.04879	42.12468	66.61083
H	29.08907	42.33828	66.57039
H	29.1594	37.55246	62.82261
N	30.03583	35.04332	63.67935
H	30.8881	35.37261	63.21632
H	29.35264	34.77193	62.96706
H	30.27283	34.21138	64.22815